Materials Chemistry and Physics 203 (2018) 106–117

Contents lists available at ScienceDirect

Materials Chemistry and Physics

journal homepage: www.elsevier.com/locate/matchemphys

Investigation of structural, electronic, anisotropic elastic, and lattice dynamical properties of MAX phases borides: An Ab-initio study on hypothetical M_2AB (M = *Ti*, *Zr*, *Hf*; A = *Al*, *Ga*, *In*) compounds

Gokhan Surucu [a, b, c, *]

[a] Ahi Evran University, Department of Electric and Energy, 40100, Kirsehir, Turkey
[b] Middle East Technical University, Department of Physics, 06800, Ankara, Turkey
[c] Gazi University, Photonics Application and Research Center, 06500, Ankara, Turkey

HIGHLIGHTS

- The structural, electronic, and lattice dynamical properties of MAX phases borides are studied.
- The calculated all M_2AB phases are mechanically and thermodynamically stable.
- The band structures for M_2AB phases are metallic in nature.

GRAPHICAL ABSTRACT

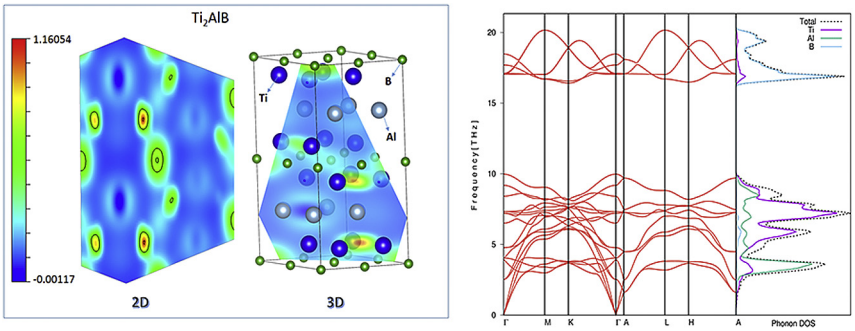

ARTICLE INFO

Article history:
Received 26 April 2017
Received in revised form
13 August 2017
Accepted 19 September 2017
Available online 20 September 2017

Keywords:
MAX phases
Electronic properties
Phonons
Mechanical properties
Elastic properties
Borides

ABSTRACT

The structural, electronic, anisotropic elastic, and lattice dynamical properties of the M_2AB (M = *Ti*, *Zr*, *Hf*; A = *Al*, *Ga*, *In*) compounds belong to the family of *MAX* phases have been investigated by accomplishing the first principles density functional theory (DFT) calculations with utilizing the generalized–gradient approximation (GGA). Structural parameters, formation enthalpies, and *X*-ray diffraction patterns have been calculated for all compounds. Electronic band structure and corresponding density of states (DOS) have been obtained. Having negative formation enthalpy showed that, all compounds could be experimentally synthesized. Also, among the nine different M_2AB compounds, the most stable one has been found as Hf_2InB with respect to the formation enthalpies and band filling theory calculations. Moreover, the elastic constants have been predicted using the stress-finite strain technique. The numerical estimations of the bulk modulus, shear modulus, Young's modulus, Poisson's ratio, Pugh's modulus, hardness, thermal conductivities, and anisotropy factors have been studied. All compounds are found to have low thermal conductivity and all compounds (except *Zr* involved ones) are hard materials and mechanically stable. Furthermore, the phonon dispersion curves as well as corresponding phonon PDOS have been plotted.

* Ahi Evran University, Department of Electric and Energy, 40100, Kirsehir, Turkey. Tel.: +90 386 280 54 00; fax:+90 386 280 54 36.
E-mail address: g_surucu@yahoo.com.

https://doi.org/10.1016/j.matchemphys.2017.09.050
0254-0584/

1. Introduction

Nano-laminated ternary compounds crystallized in hexagonal $P6_3/mmc$ structure with the $M_{(n+1)}AX_n$ formula are named as the *MAX* phases, where *M* is an early transition metal, *A* is a group *A* element and *X* is the carbon (*C*) and/or nitrogen (*N*) atom [1]. These compounds have different stoichiometries with respect to varying of *n* values from 1 to 3 [2,3]. It is also known that, there are higher order *MAX* phases for $n = 4–6$ [4]. In the *MAX* crystal, $M_{(n+1)}X_n$ ceramic slabs are separated from each other by a pure *A* (metallic) layer, which causes to an inherently laminated structure with a mixture of strong *M-X* bonds and weaker *M-A* bonds [5–9]. This anisotropic hexagonal structure of the *MAX* phases leads to a unique combination of ceramic and metallic properties such as high strength and stiffness at high temperatures, oxidation and thermal shock resistance, good damage tolerance, good corrosion resistance and good thermal and electrical conductivity [8–12]. These challenging properties make *MAX* phases a popular in the industrial and technological applications such as Li-ion batteries [6], wear and corrosion resistant coatings [13], superconducting materials [14], spintronics [15] and nuclear industry [16,17].

Recently, the researchers have focused on improving the diversity and performance of the *MAX* phase materials according to the needs. These studies could be vary as the discovery of new *MAX* phases and the mixture of existing phases [9,18–24]. The studies also have been done to find out the effects of point defects and atom incorporation on the properties of *MAX* phases [25–28]. In addition, 211 and 312 phases of Ti-Al systems for a mixture of *C* and *N* atoms, namely $Ti_2Al(C_{0.5}N_{0.5})$ and $Ti_3Al(C_{0.5}N_{0.5})_2$ have been studied in the literature [29–31].

However, the common point of all the studies done to date is to leave *X*-site atom as *C* and/or *N* while focusing on *M*- and A-site atoms except the study done by Khazaei *et. al.* in which the X-site atom is replaced with Boron *(B)* [32]. In that theoretical work, the electronic and mechanical properties of M_2AlB (A = *Al*; M = *Sc, Ti, Cr, Zr, Nb, Mo, Hf, Ta*) have been compared with that of the M_2AlC and M_2AlN. As they have noted, further theoretical research is demanded the borides of *MAX* phases. Additionally, *B* and its compounds are challenging materials with respect to their interesting physical, chemical and mechanical properties and they have a wide potential in engineering applications [33]. Therefore, the synthesizable of $M_{n+1}AB_n$ compounds and how the properties of these compounds differ from the conventional *MAX* phases are an attractive topic.

In this study, *ab-initio* calculations for nine different *M-A combinations for MAX–borides (M_2AB, where M = Ti, Zr, Hf and A = Al, Ga, In)* compounds have been investigated. In this context, the results are discussed in three main sections. Firstly, structural and electronic properties of the M_2AB compounds have been discussed. Secondly, elastic parameters have been detailed to show the mechanical properties of the material such as hardness, stability, and stiffness which are crucial particularly for industrial and technological applications. Moreover, the directional dependence of anisotropic elastic properties, compressibility, Poisson ratio, Young's and Shear moduli have been studied. Then, phonon dispersion curves, and thermal conductivities of the corresponding phases have been analyzed. Brillioin zone-center phonon frequencies for Γ point which are Raman Active Modes, Hyper Raman Active Modes, and Infrared Active Modes have been obtained.

2. Calculation methods

In the present paper, the calculations have been performed using the Vienna Ab-initio Simulation Package (VASP) [34,35] based on the density functional theory (DFT). The electron-ion interaction was taken into consideration in the form of the projector-augmented-wave (PAW) method with plane wave up to energy of 550 eV [36,37]. For the exchange and correlation terms in the electron-electron interaction, Perdew-Burke-Ernzerhof (PBE) functional [38] was used within the generalized gradient approximation (GGA). Convergence tests were performed with respect to the Brillouin zone (BZ) sampling and the size of the basis set. The converged result was achieved with 16 × 16 × 4 k-point mesh which has been used in the irreducible Brillouin zone yielding 90 k-points centered at Γ-point for M_2AB compounds. The special k-point mesh was produced by using the Gamma centered grid [39].

In order to determine the ground state geometries for M_2AB compounds, the conjugate gradient algorithm with force convergence less than 10^{-8} eV $Å^{-1}$ was used by minimizing stresses and Hellman–Feynman forces. The energy tolerance was less than 10^{-9} eV per unit cell in the iterative solution of the Kohn–Sham equations. All steps were carried out by using Methfessel–Paxton method [40] in the order of 1 for all relaxation schemes. Then the tetrahedron method with Blöchl corrections [41] were applied to obtain accurate energy values. The valence electron configurations of *Ti, Zr, Hf, Al, Ga, In* and *B* atoms are considered as $3d^34s^1$, $4s^24p^65s^24d^2$, $5d^26s^2$, $3s^23p^1$, $4s^24p^1$, $5s^25p^1$ and $2s^22p^1$, respectively.

The elastic constants (C_{ij}) have been computed by using the strain–stress method implemented in VASP [34,35,42].

The phonon band structure and phonon density of states was obtained with the PHONOPY software package from force constant matrices calculated using the VASP implementation of density functional perturbation theory (DFPT) [43,44]. Sufficient convergence with respect to the forces was reached for a 2 × 2 × 1 (32 atoms with a 8 × 8 × 4 k-mesh) supercell. The same cutoff value was used in DFPT calculation.

Additionally, X-ray diffraction patterns are obtained by using VESTA program package [45] and the Cu Kα source having the wavelength of 1.541 Å is used.

3. Results and discussion

3.1. Structural and electronic properties

The phase of M_2AB (*M = Ti, Zr, Hf; A = Al, Ga, In*) crystallize in a hexagonal structure with the space group $P6_3/mmc$, in which the *M* atom occupies at 4f (1/3, 2/3, z), *A* at 2d (1/3, 2/3, 3/4), and *B* at 2a (0, 0, 0) Wyckoff positions.

As seen in Fig. 1, M_2AB compounds crystallize with ceramic-like strongly bonded *M-B* atomic layers and interleaved *A* layers. Structural optimizations are carried out by taking into account lattice parameters. The calculated lattice parameters (a, c) and z-internal parameters are listed in Table 1.

The obtained results for the *A = Al* involved compounds are agree well with previous theoretical report [32]. Since there are no studies for borides compounds of hypothetical *MAX* phases, The obtained results apart from the *Al* involved compounds are compared with the results for including *X = C* and *N* the compounds [1,5,11,32].

As seen from Table 1 that the lattice constants increase as one goes from *N*-containing compounds to *B*-containing compounds (*N→C→B*) in accordance with the mass of the anions while the densities decrease. Due to the calculations, the largest value of density (10.435 g/cm^3) is obtained for Hf_2InB.

Formation enthalpies for M_2AB compounds are also calculated by using the following relation:

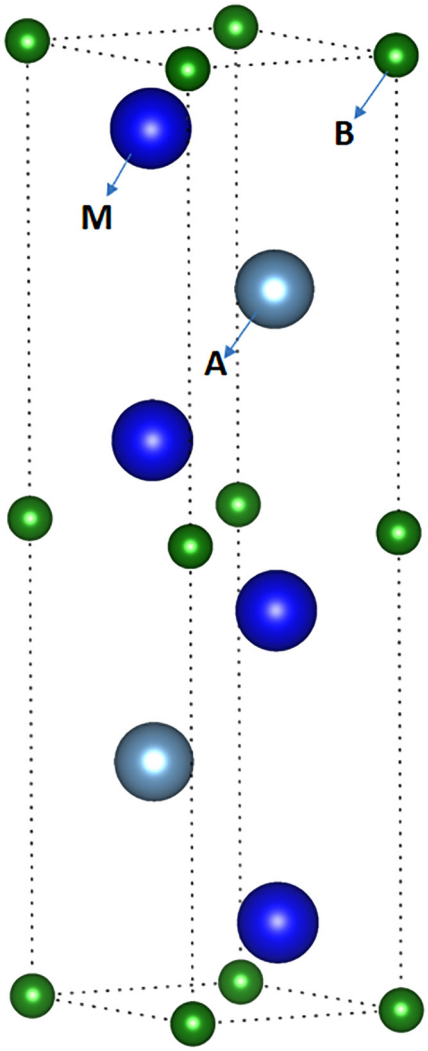

Fig. 1. The crystal structure of M_2AB compounds.

$$E_{form}^{M_2AB} = E_{Total}^{M_2AB} - 2E_{Solid}^{M} + E_{Solid}^{A} + E_{Solid}^{B} \quad (1)$$

where E_{Solid}^{M}, E_{Solid}^{A} and E_{Solid}^{B} are calculated from M_2AB ($M = Ti, Zr, Hf$; $A = Al, Ga, In$; and B) structures, respectively. All M_2AB compounds are thermodynamically stable owing to the negative formation enthalpy values as given in Table 1 which indicates that they should be possible to synthesize the considered phases. Additionally, more negative formation enthalpy usually corresponds to a better stability. Among these phases, Hf_2InB (−4.162 eV/atom) is found to be relatively the most stable one.

The band structures for M_2AB are predicted along the high symmetry directions in the first Brillouin zone from the calculated equilibrium lattice constant. The band structures and corresponding partial and total electronic density of state (DOS) are displayed for Hf_2InB in Fig. 2 a only to save space in the journal. Additionally the total DOS for all compounds due the varying of M are given in Fig. 2b. As seen from the figure, the DOS values vary from zero at the Fermi level which indicates that all compounds are metallic. The most significant contribution to DOS comes from transition metals d-states at the locality of the Fermi level. The variation of electron numbers at fermi levels are given in Table 1. Having the lowest electron number demonstrates the most stability structure which is also consistent with the estimation from formation enthalpy of Hf_2InB ($n = 1.734$).

In addition, there is a strong hybridization, which point outs the presence of covalent interactions, between s, p and d orbitals at the delocalized bands in the energy range of −6 and −2 eV and the strong hybridization exists between p and d orbitals in the energy range of −2 and 0 eV. Moreover the delocalized bands in the energy range from 0 to 4 eV are dominated by d orbital for all phases. Besides, a pseudo gap exists near the Fermi energy for all phases and it separates the bonding and antibonding states.

On the other hand, the stability of the compounds by means of band filling theory could be discussed with the help of DOS curves [46,47]. According to band filling theory; when the numbers of bonding (anti-bonding) states increase (decrease), there is an increment in the stability of the material. Hence, the ratio W_{occ} (the width of the occupied states)/W_b (the width of the bonding states) could give information about the electronic stability of the material.

Table 1
The calculated equilibrium lattice parameters (a, and c in Å), Wyckoff positions internal parameter (z), density (ρ in g/cm^3), formation energies (ΔH_f in eV/atom), electron numbers at fermi level (n), the width of occupied states (W_{occ} in eV), bonding states (W_b in eV), and the scattering angle (2Θ) for preferred orientation [002] of M_2AB.

Compounds	Reference	a	c	z	ρ	ΔH_f	n	W_{occ}/W_b	2Θ
Ti_2AlB	Present	3.148	14.064	0.087	3.673	−3.577	2.277	1.006	12.587
	Theory [32]	3.148	14.077		3.672				
Ti_2AlC	Theory [1]	3.040	13.600		4.110				
	Theory [5]	3.071	13.726						
	Theory [32]	3.069	13.737		3.995				
Ti_2AlN	Theory [1]	2.989	13.614		4.310				
	Theory [5]	2.998	13.634						
	Theory [32]	2.999	13.643		4.283				
Ti_2GaB	Present	3.159	13.770	0.088	4.919	−3.541	2.231	1.000	12.847
Ti_2GaC	Theory [1]	3.070	13.520		5.530				
Ti_2GaN	Theory [1]	3.000	13.300		5.750				
	Theory [11]	3.020	13.301	0.092					
Ti_2InB	Present	3.228	14.534	0.081	5.606	−3.448	2.430	1.002	12.169
Zr_2AlB	Present	3.407	14.895	0.089	4.882	−3.800	4.741	1.031	11.873
	Theory [32]	3.408	14.863		4.893				
Zr_2AlC	Theory [32]	3.320	14.618		5.269				
Zr_2AlN	Theory [32]	3.252	14.422		5.617				
Zr_2GaB	Present	3.423	14.480	0.092	5.942	−3.785	5.670	1.043	12.215
Zr_2InB	Present	3.453	15.435	0.084	6.416	−3.735	3.241	1.021	11.457
Hf_2AlB	Present	3.363	14.711	0.088	9.096	−4.073	2.536	1.001	12.022
	Theory [32]	3.365	14.675		9.111				
Hf_2AlC	Theory [32]	3.273	14.401		9.846				
	Theory [32]	3.192	14.307		10.471				
Hf_2GaB	Present	3.376	14.339	0.090	10.265	−4.140	3.092	1.000	12.335
Hf_2InB	Present	3.414	15.215	0.083	10.435	−4.162	1.734	1.000	11.623

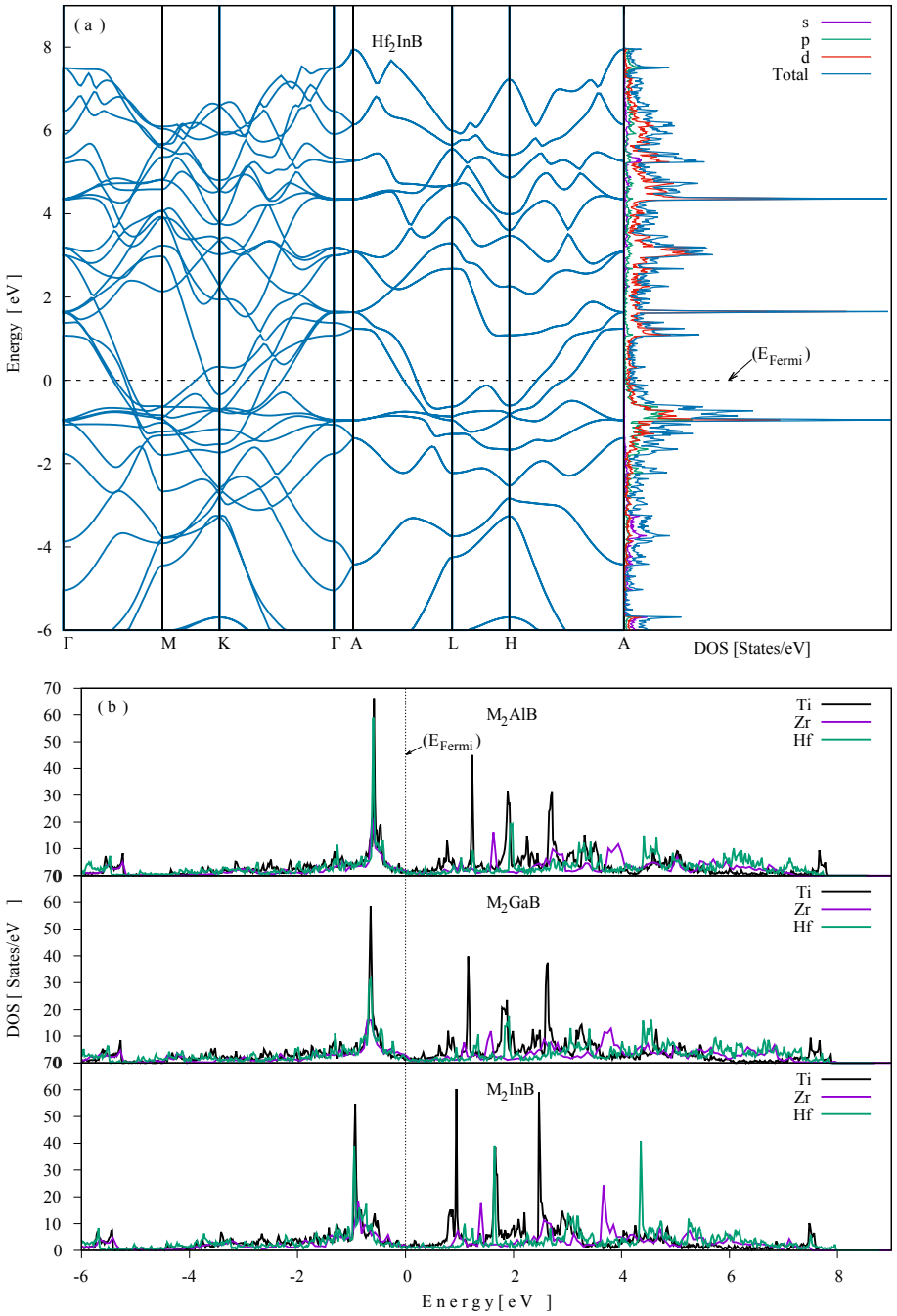

Fig. 2. Calculated the electronic band structure and the corresponding PDOS of the *Hf_2InB* (a) and TDOS of the *M_2AB* compounds (b).

If the value of this ratio is closer to 1.0, the stability increases. W_{occ}/W_b values for all phases are given in Table 1. The ratios of W_{occ}/W_b are almost 1.0 for $M = Ti$ and *Hf* involved compounds, while they are very close to 1.0 for $M = Zr$ involved compounds. These results indicate that *Zr* involved compounds have higher antibonding states than the other compounds.

The charge densities for all phases are calculated. Due to the calculations, all phases dominantly having ionic bonding for all phases. Moreover, extra covalent contribution is observed for *Ti* and *Hf* involved compounds with the help of the charge density maps which are plotted in (111) plane as shown in Fig. 3. In order to show the bonding more clearly, Fig. 3 is illustrated in 2 × 2 × 1 supercell. These maps are given just for *Ti_2AlB* (Fig. 3a) and *Zr_2GaB* (Fig. 3b) to save space in the journal.

The characteristics of *X*-ray diffraction patterns give significant information about the structural properties of materials such as crystallinities. *X*-ray diffraction patterns for each compounds are given in Fig. 4 and the corresponding scattering angles (2Θ) belong to the preferred orientations along [002] are also given in Table 1. Fig. 4 reveals that, M = *Zr* involved compounds have polycrystalline tendency while the other compounds have single crystalline structure. It could be deduced that having the highest electron numbers at fermi levels and the increase in antibonding states lead to polycrystalline nature.

3.2. Mechanical properties

Elastic constants (C_{ij}) are the keystones to determine the

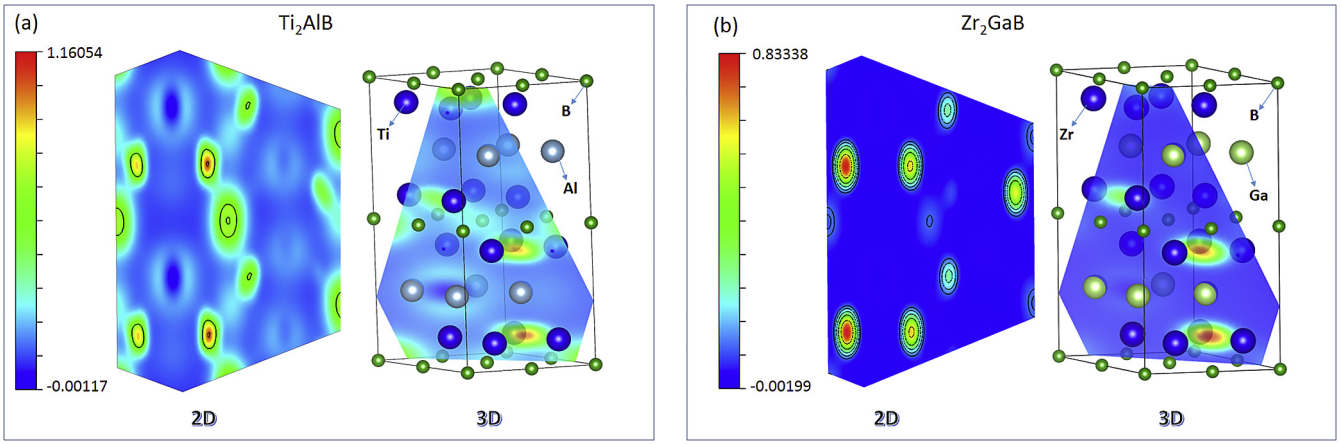

Fig. 3. Calculated valence charge density of *Ti₂AlB* (a) *and Zr₂AlB* (b).

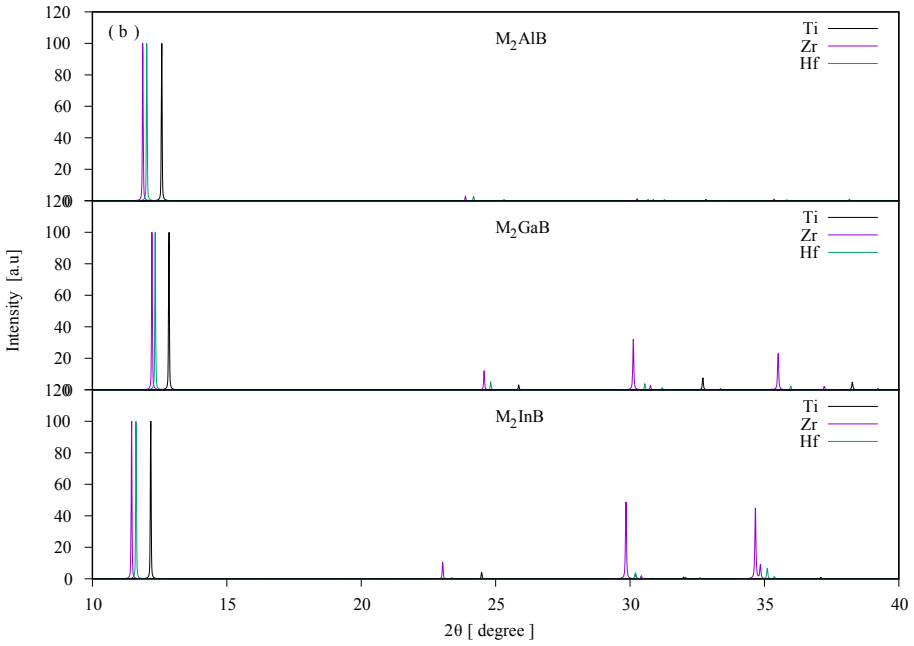

Fig. 4. Calculated the *X*-ray diffraction patterns of the *M₂AB* compounds.

mechanical and dynamical behavior of the material. And they are important to be known for any technological applications. In order to reveal the information about the material's hardness, stability and stiffness, the elastic constants of a hexagonal structure which are C_{11}, C_{12}, C_{13}, C_{33}, and C_{44} are obtained and these values are given in Table 2. Additionally, the obtained results along with the theoretical values in literature [32] for *Al* involved compounds are also given in the Table. The comparison of these results revealed that the calculated elastic constants for *Zr₂AlB* are coherent. On the other hand, the obtained results for C_{11}, C_{13}, C_{33}, C_{44} values are lower (about 16–34%) and C_{12} value is higher (about 17%) than the theoretical values in literature for other *Al* involved compounds [32]. These differences may stem from the differences in between the used calculation techniques.

The durability of the crystal against external forces, which is also called as the mechanical stability of a crystal, is a desired property to check its sustainability in any application. Mechanical stability is checked due to the Born-Huang criteria [48]. The obtained results satisfy these conditions. So it can be said that all possible M_2AB crystal structures are mechanically stable.

From Table 2, it is also easily seen that *Al* involved compounds have the largest C_{11}, C_{13}, C_{33}, and C_{44}, while *Ti₂GaB* has the largest C_{12}. Also, C_{11} is higher than C_{33} for M_2AB apart from *Ti₂AlB* and *Hf₂AlB*. $C_{11} > C_{33}$ shows that the incompressibility along the $[10\bar{1}0]$ and $[01\bar{1}0]$ directions is stronger than that along the [0001] direction and implies the bonding strength along the $[10\bar{1}0]$ and $[01\bar{1}0]$ directions is stronger than that along the [0001] direction. In addition, $C_{11}+C_{12}$ is larger than C_{33} for all M_2AB compounds. This indicates that the resistance to the elastic deformation is higher in the (0001) plane than along the c-axis [49].

In order to calculate the Bulk (B) and Shear (G) moduli due to the Voigt-Reuss-Hill (VRH) approximations, elastic constants have been used [44,45]. Here, Voigt bound refers the upper limit while Reuss bound refers the lower of the moduli considering a strain uniformly throughout the crystal. Hill approximation is generally used to get adequate views for elastic parameters of polycrystalline materials utilizing arithmetic mean of the Voigt and Reuss limits as given below;

Table 2
The calculated Elastic constants (C_{ij}, in GPa) for M_2AB.

Compounds	Reference	C_{11}	C_{12}	C_{13}	C_{33}	C_{44}
Ti_2AlB	Present (stress-strain)	233.971	73.901	80.596	261.885	115.072
	Theory [32] (volume conserving)	196.393	87.076	57.977	208.973	75.348
Ti_2GaB	Present (stress-strain)	210.317	81.161	58.238	205.911	72.483
Ti_2InB	Present (stress-strain)	203.047	72.789	49.183	189.981	59.026
Zr_2AlB	Present (stress-strain)	173.851	71.971	50.775	167.195	53.283
	Theory [32] (volume conserving)	176.728	70.036	51.398	175.690	52.037
Zr_2GaB	Present (stress-strain)	178.005	69.875	65.495	128.046	50.692
Zr_2InB	Present (stress-strain)	184.168	61.943	45.521	174.291	44.966
Hf_2AlB	Present (stress-strain)	232.240	71.838	81.023	266.583	108.817
	Theory [32] (volume conserving)	203.755	76.472	58.480	199.766	67.518
Hf_2GaB	Present (stress-strain)	213.380	76.755	62.588	176.322	66.005
Hf_2InB	Present (stress-strain)	209.852	68.702	49.953	196.883	55.330

$$B = (B_V + B_R)/2, \quad G = (GV + GR)/2 \tag{3}$$

Here, Voigt and Reuss bounds represent V and R subscripts respectively. For each crystal structure, the inclusive expressions of these bounds are obtained from their own elastic constants [48,50]. Additionally, Young's modulus (E) and Poisson's ratio (ν) have been obtained from above-referred B and G values using following relations;

$$E = 9BG/(3B + G), \quad \nu = (3B - 2G)/[2(3B + G)] \tag{4}$$

Bulk modulus identifies the material's incompressibility property. In other words, it measures the resistance to the change in the volume without a shape deformation when the material is exposed to hydrostatic pressure. Shear modulus measure the resistance to change in a shape at constant volume. Generally, the directional bonding occurs between atoms where electron density is geometrically localized when the shear modulus has the higher values. Therefore, more energy is required to break these bonds. And the material is assumed as more rigid. Furthermore, Young's modulus supplies a measure of stiffness of solid [51,52].

The calculated Bulk moduli (B), Shear moduli (G), Young's moduli (E), Poisson's ratio (ν), Pugh's modulus (G/B), and Vickers hardness (H_V) for M_2AB are listed in Table 3. M_2AlB phases have the highest B, G and E values for $M = Ti$ and Hf involved compounds. It is concluded that M_2AlB is the lowest compressible and highest stiffness one among the Ti_2AB and Hf_2AB compounds.

Additionally, the obtained results along with the theoretical values in literature [32]for Al involved compounds are also given in Table 3. The calculated results for Ti_2AlB and Hf_2AlB compounds are higher than ref [32], while the calculated results for Zr_2AlB are coherent. These differences in the B, G and E values of Ti_2AlB and Hf_2AlB compounds are due to the fact that the calculated elastic constants are incompatible with the results of Ref. [32].

Also, the B, G and E values are compared according to the each M = Ti, Zr and Hf involved compounds. It is deduced that, Al involved compounds have the highest values, while In involved compounds have the lowest values for the compounds of $M = Ti$ and Hf. On the contrary, there is not such a tendency for the compounds of M = Zr. This could be explained via Cauchy pressure which is defined as (C_{12}−C_{66}) and (C_{13}−C_{44}) for hexagonal materials. The positive value of Cauchy pressure brings out damage tolerance and ductility of a crystal, while the negative one shows brittleness. The calculated Cauchy pressures for the compounds of M = Zr are positive or about positive, while they are negative for the compounds of M = Ti and Hf. It can be said that the compounds of $M = Zr$ have brittleness behavior and the compounds of M = Ti and Hf have ductility behavior. The same result can also be supported by B/G ratio, which is defined as the indicator of ductility or brittleness of a material. The values of the ratio is higher than 1.75 refer ductility, while lower values indicate brittleness. The B/G values are found to be less than 1.75 for the compounds of $M = Ti$ and Hf, while they are higher than 1.75 for the compounds of $M = Zr$ as given in Table 3.

Relatedly, G/B ratio (Pugh's modulus) is the parameter which is used to find the bonding characters of the atoms in the crystal. When the value of Pugh's modulus is around 1.1, covalent bonding is more dominant than ionic bonding. On the contrary, Pugh's modulus is around 0.6 indicates that the opposite situation is valid [52]. As seen in Table 3, all the values are around 0.6 that is the indication of the ionic bonding is dominant in the structure. The present values of $G/B \approx 0.6$ strongly support the ionic contribution to inter-atomic bonding. On the other hand, the values of G/B are more close to 0.6 which states a tendency from covalent to ionic contribution to the inter-atomic bonding, particularly for Ti and Hf involved compounds.

The above-stated bonding nature of the M_2AB is verified by the values of Poisson's ratio (ν) as well. According to the studies in the

Table 3
The calculated bulk modulus (B, in GPa), Shear Modulus (G, in GPa), Young's modulus (E in GPa), Poisson's ratio (ν), and Hardness (H_v, in GPa) for M_2AB compounds.

Compounds	Reference	B	G	E	ν	B/G	G/B	H_V
Ti_2AlB	Present	134.020	93.580	227.398	0.215	1.420	0.703	16.321
	Theory [32]	111.915	66.752	167.045	0.251			
Ti_2GaB	Present	113.297	70.312	174.700	0.243	1.613	0.619	10.813
Ti_2InB	Present	103.882	64.618	160.492	0.242	1.608	0.621	10.224
Zr_2AlB	Present	95.510	53.910	136.302	0.262	1.768	0.565	7.650
	Theory [32]	97.092	55.018	138.831	0.262			
Zr_2GaB	Present	97.031	49.506	126.920	0.282	1.959	0.510	5.922
Zr_2InB	Present	94.018	53.501	138.701	0.254	1.699	0.588	8.234
Hf_2AlB	Present	132.691	91.690	223.489	0.219	1.447	0.691	15.222
	Theory [32]	110.340	67.204	167.588	0.247			
Hf_2GaB	Present	111.098	66.698	166.700	0.250	1.664	0.600	9.792
Hf_2InB	Present	105.701	65.402	162.605	0.243	1.616	0.618	10.381

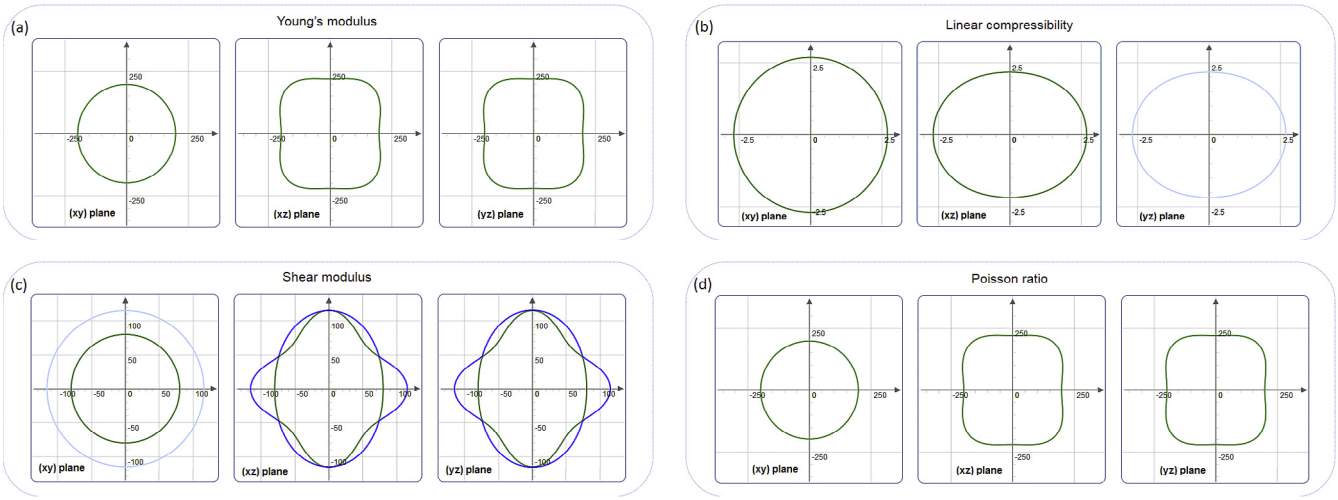

Fig. 5. The calculated directional dependence of the mechanical properties; Young's modulus (a), linear compressibility (b), Shear Modulus (c), Poisson's ratio (d) for M_2AB compounds.

literature, the small values about 0.1 correspond to the covalent materials while the typical value of ν is 0.25 for ionic materials [52]. In Table 3, all the ν values are about 0.25 implying that the bonding character of the structure is ionic bonds which can be also easily seen in charge maps (in Fig. 3).

As the last parameter in Table 3, hardness has been calculated by using the semi-empirical method based on Pugh's modulus ratio developed by Chen et al. [53] as given below;

$$H_V = 2\left(k^2 G\right)^{0.585} - 3; \quad (k = G/B) \tag{5}$$

Here, the parameter k is the Pugh's modulus ratio.

As shown in Table 3, in M_2AB phases, Ti_2AlB has the highest hardness (16.321 GPa), while Zr_2GaB has the lowest (5.922 GPa). Actually, the calculated hardness values for all of M_2AB are under the superhardness limit ($H_V \geq 40$ GPa), indicating that these compounds except for *Zr* involved compounds and Hf_2GaB are relatively hard materials.

The anisotropy of elasticity has a significant function to determine the technological usage of the material with the having effects on the physical or mechanical properties such as unusual phonon modes, dislocation dynamics, precipitation, anisotropic plastic deformation and etc. [54]. Moreover, formation of micro-cracks originated from the elastic anisotropy is also important to be understood to enhance the mechanical durability of the material in any application [55]. Therefore, anisotropy calculations are essential to get a complete elastic analysis of the material.

Here to visualize and calculate the directional dependence of the Young's modulus, linear compressibility, Shear modulus, and Poisson ratio, ElAM code [56] has been used. In the plots of these physical properties, the degree of anisotropy is indicated by the deviation from the spherical shape. These parameters along the crystallographic directions (in 2D) have been given just for Ti_2AlB in Fig. 5 to save space in the journal. In addition, the maximum and minimum values of these parameters are listed in Table 4 for all compounds.

According to Fig. 5, all the parameters possess obvious anisotropy as follows; Young's modulus (Fig. 5a) and linear compressibility (Fig. 5b) in (*xy*) plane for M_2AB exhibiting to be more isotropic than (*xz*) and (*yz*) plane. It is known that *z*-axis is more compressible than the *x*-axis when the C_{11} larger than the C_{33}. Excluding Ti_2AlB and Hf_2AlB from M_2AB compounds have the C_{11} larger than the C_{33}. Also, in (*xz*) plane, the deviation from the axes in at an angle of 45° indicates that Young's modulus has its maximum.

As seen in Fig. 5 c, shear modulus has the maximum values on the axes in both the (*xz*) and (*yz*) planes while it becomes smaller with a 45° deviation from these axes. Moreover, it looks like isotropic in (xy) plane.

A more complicated anisotropy is seen for Poisson's ratio in (*xy*) and (*xz*) plane. In contrast, there are not any isotropic behaviors of ν in the rest of the planes.

Anisotropic factors (A_1, A_2, A_3) have been calculated with the following equations which were referred to the most useful ones

Table 4
Maximum and minimum values of Young's modulus (E_{max} and E_{min}, in GPa), linear compressibility (β_{max} and β_{min}, TPa^{-1}), Shear moduli (G_{max} and G_{min}, in GPa), and Poisson's ratio (ϑ_{max} and ϑ_{min}) of M_2AB.

Compounds	Young's Modulus		Linear Comp.		Shear Modulus		Poisson Ratio	
	E_{min}	E_{max}	β_{min}	β_{max}	G_{min}	G_{max}	ϑ_{min}	ϑ_{max}
Ti_2AlB	197.67	252.56	2.17	2.68	1.00	115.10	0.09	0.30
Ti_2GaB	172.26	182.64	2.77	3.29	1.00	74.25	0.19	0.33
Ti_2InB	150.85	172.45	2.96	3.73	1.00	72.96	0.18	0.32
Zr_2AlB	132.94	146.21	3.24	4.01	1.00	59.18	0.20	0.36
Zr_2GaB	93.39	135.90	2.70	5.05	1.00	54.05	0.22	0.38
Zr_2InB	122.84	157.80	3.32	4.00	1.00	66.51	0.17	0.36
Hf_2AlB	196.86	246.48	2.09	2.73	1.00	108.80	0.12	0.29
Hf_2GaB	149.29	175.59	2.62	3.81	1.00	68.30	0.22	0.29
Hf_2InB	147.16	181.30	2.95	3.58	1.00	76.28	0.18	0.33

Table 5
Shear anisotropic factors (A_1, A_2, and A_3), the percentage (in %) of anisotropy in the compression and shear (A_B and A_G), and universal anisotropic index (A^U) for M_2AB.

Compounds	A_1	A_2	A_3	A_B	A_G	A^u
Ti_2AlB	1.380	1.501	1.269	0.013	0.025	0.505
Ti_2GaB	0.967	0.953	0.982	0.014	0.026	0.521
Ti_2InB	0.802	0.767	0.838	0.015	0.028	0.564
Zr_2AlB	0.890	0.866	0.915	0.016	0.026	0.593
Zr_2GaB	1.197	0.901	1.621	0.017	0.019	0.459
Zr_2InB	0.673	0.649	0.698	0.017	0.017	0.453
Hf_2AlB	1.299	1.439	1.173	0.021	0.017	0.480
Hf_2GaB	1.008	0.875	1.161	0.023	0.018	0.572
Hf_2InB	0.722	0.692	0.753	0.024	0.023	0.711

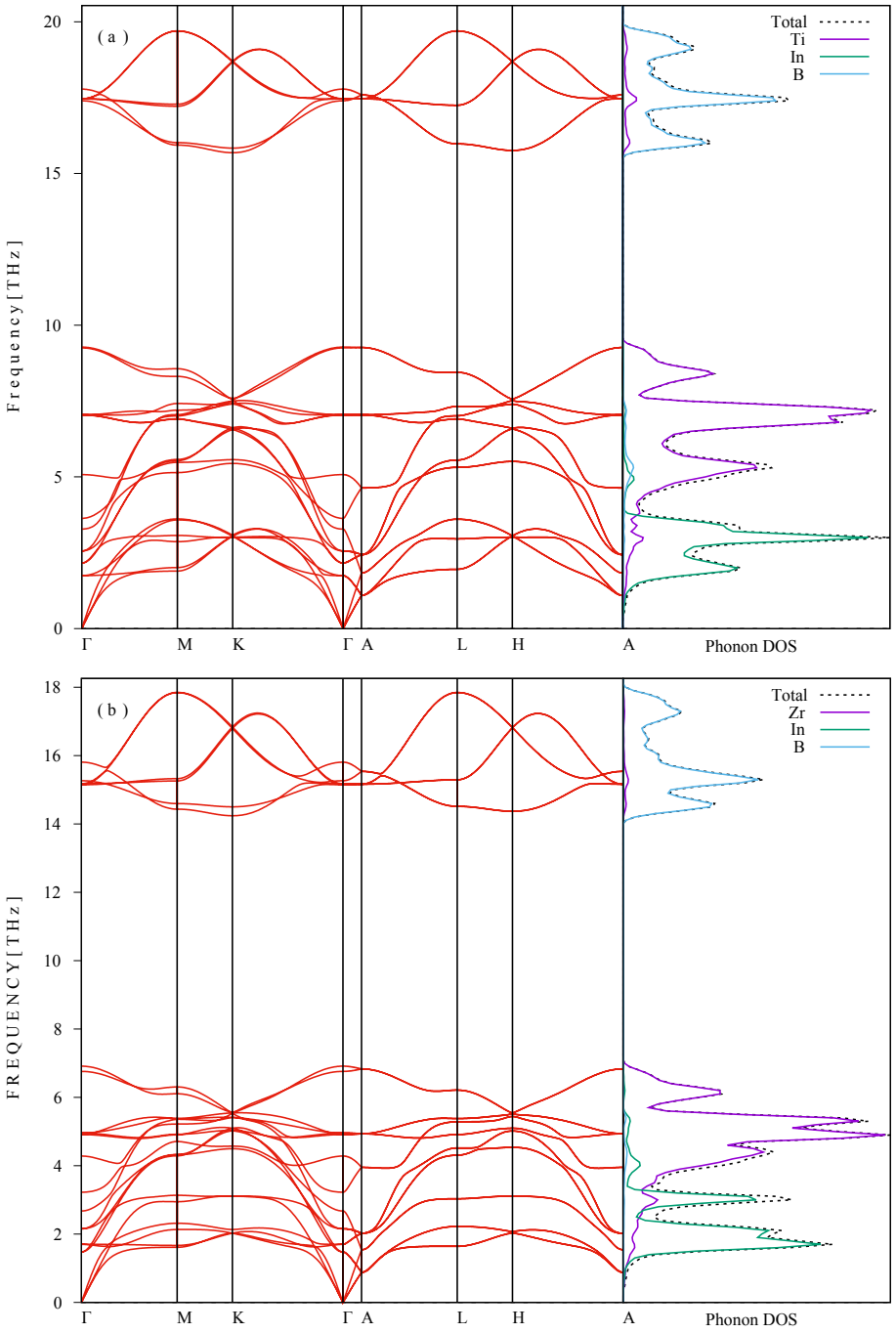

Fig. 6. Phonon dispersion curves and PDOS of the Ti_2InB (a), Zr_2InB (b), Hf_2InB (c), and phonon TDOS of the M_2AB compounds (d).

for providing in-plane phonon-focusing information for hexagonal crystals [57].

$$A_1 = \frac{C_{44}\,(C_{11} + 2C_{13} + C_{33})}{\left(C_{11}C_{33} - C_{13}^2\right)} \quad \text{for} \quad [001] \tag{6}$$

$$A_2 = \frac{2C_{44}}{(C_{11} - C_{13})} \quad \text{for} \quad [100], (010) \tag{7}$$

$$A_3 = \frac{2C_{44}}{(C_{33} - C_{13})} \quad \text{for} \quad [001], (010) \tag{8}$$

Here, symmetry axis and plane is represented with the [*ijk*] and (*ijk*), respectively. A_1, A_2, A_3 values are one for a completely isotropic material. On the other hand, a deviation from one relates to an elastic anisotropy. And, positive smaller or grater values of A_2 and A_3 point in-plane focusing or defocusing, respectively. The anisotropic factors are calculated as given in Table 5. And as seen in the table, all values deviate from one which refers to the anisotropic

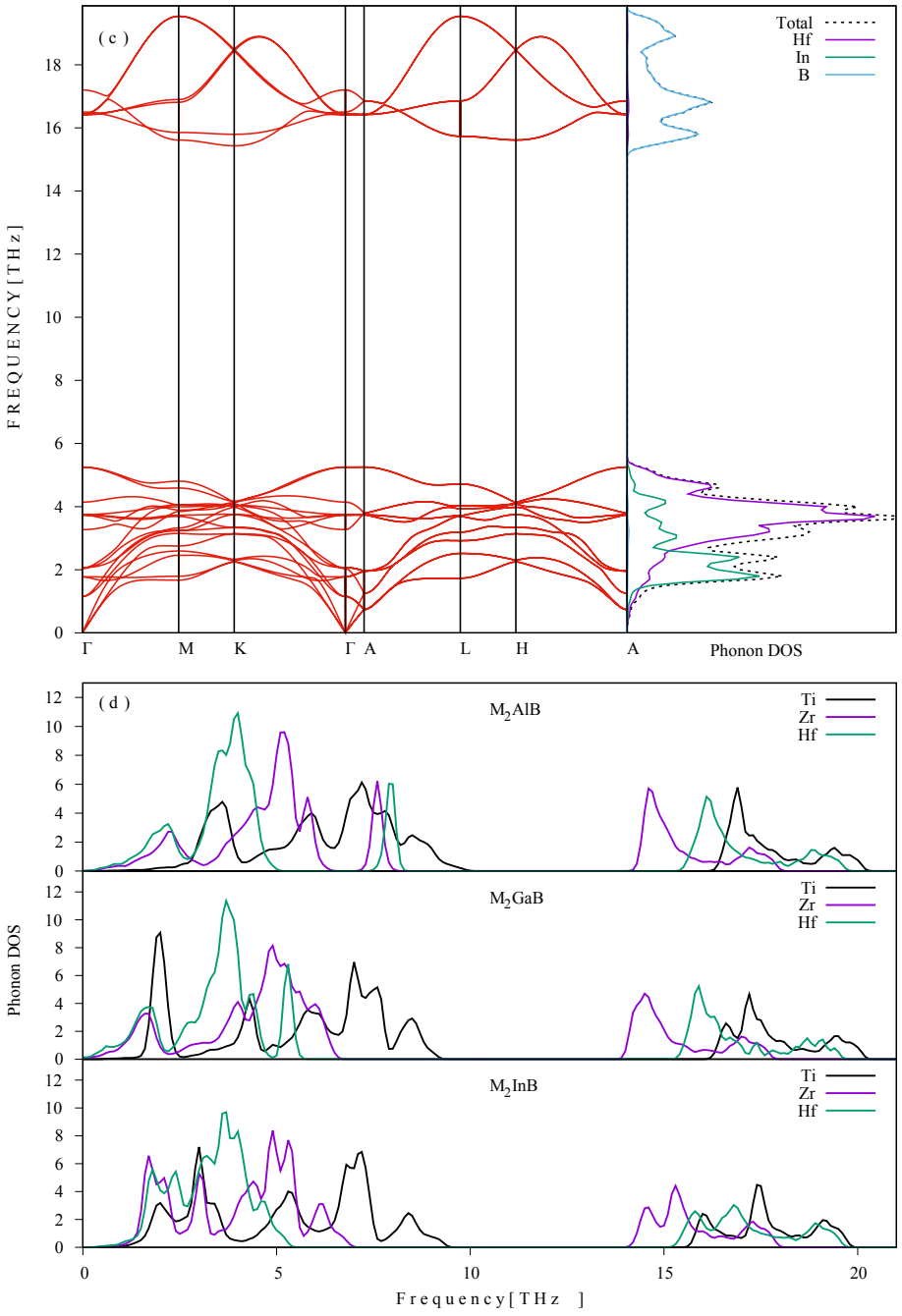

Fig. 6. (*continued*).

mechanic characteristics of M_2AB compounds. The universal anisotropy index (A^U) and percent elastic anisotropy in shear and compression (A_G, A_B) are also calculated with the following relations given in Ref. [58].

$$A^U = 5(G_V/G_R) + (B_V/B_R) - 6 \quad (9)$$

$$A_G = (G_V - G_R)/(G_V + G_R) \quad (10)$$

$$A_B = (B_V - B_R)/(B_V + B_R) \quad (11)$$

Table 5 reveals the calculated results for A^U, A_G, and A_B. The universal index and percent anisotropy in shear and compression

Table 6
The calculated minimum thermal conductivities for M_2AB.

Compounds	Clarke model		Cahill model	
	M_a (10^{-26})	λ_{min} ($W_m^{-1}K^{-1}$)	n (10^{28})	λ_{min} ($W_m^{-1}K^{-1}$)
Ti_2AlB	5.544	1.547	6.600	1.684
Ti_2GaB	7.318	1.183	6.700	1.293
Ti_2InB	9.190	0.996	6.100	1.088
Zr_2AlB	9.142	0.900	5.300	0.988
Zr_2GaB	10.917	0.797	5.400	0.880
Zr_2InB	12.789	0.760	5.000	0.832
Hf_2AlB	16.388	0.866	5.500	0.943
Hf_2GaB	18.162	0.713	5.600	0.780
Hf_2InB	20.034	0.661	5.200	0.723

Table 7
The calculated phonon frequencies (THz) at Γ point of M_2AB.

Symmetry	Ti_2AB			Zr_2AB			Hf_2AB		
	Al	*Ga*	*In*	*Al*	*Ga*	*In*	*Al*	*Ga*	*In*
E_{2u}	2.524	2.415	2.159	1.654	1.592	1.477	1.324	1.262	1.155
E_{2g}	4.036	2.466	1.745	3.670	2.324	1.700	3.354	2.472	1.775
E_{1u}	4.777	3.251	2.558	4.149	2.735	2.154	4.399	2.764	2.070
B_{1u}	3.906	3.773	3.633	2.581	2.556	2.675	2.035	1.987	2.032
B_{2g}	6.505	4.437	3.280	5.504	4.215	3.224	4.353	3.921	3.272
A_{2u}	8.408	6.061	5.075	7.249	5.116	4.284	7.600	5.146	4.143
E_{1g}	7.206	7.066	7.041	4.926	4.862	4.912	3.733	3.672	3.731
E_{2g}	7.322	7.089	7.050	5.157	4.816	4.958	4.594	3.728	3.746
B_{2g}	9.974	9.165	9.278	7.920	6.458	6.759	8.074	5.556	5.252
A_{1g}	9.183	9.138	9.251	6.406	6.252	6.913	4.931	4.854	5.248
E_{2u}	17.044	17.120	17.463	14.471	14.428	15.149	15.559	15.476	16.407
E_{1u}	17.106	17.191	17.459	14.483	14.388	15.180	15.638	15.483	16.438
A_{2u}	17.697	17.712	17.396	15.026	14.833	15.265	16.471	16.304	16.503
B_{1u}	18.474	18.411	17.781	15.682	15.440	15.808	17.349	17.265	17.201

are chosen as zero for isotropic materials, Zero value of A (B_R=B_V) is related with complete elastic isotropy, while a value of 100% is related with the largest anisotropy.

3.3. Lattice dynamical properties

The phonon frequencies and phonon dispersion curves are calculated by using the supercell approach with the linear response method to check the dynamical stabilities of M_2AB phases. The obtained phonon dispersion curves with the corresponding phonon density of state are shown in Fig. 6. The phonon dispersion curves and corresponding partial and total density of state (DOS) are displayed in Fig. 6a-c for M_2InB (M = *Ti, Zr,* and *Hf)* compounds only to save space in the journal. Additionally, the total phonon DOS for all phases due the varying of M are shown in Fig. 6 d.

There are 24 branches in the phonon graph consisting of 3 acoustic and 21 optic branches with respect to having 8 atoms in the primitive cell. In acoustic branches, no soft mode is observed thus it indicates the dynamically stability of M_2AB phases.

The sharp peaks in the phonon DOS conform to the flat modes of the phonon dispersion curves. When these four graphics are analyzed together, it is seen that the dominant contribution to the acoustic branches comes from the M and A atoms. Noticeably, the main contribution comes from A atoms. The observation of acoustic branches in the lower frequencies is the indication of low lattice thermal conductivity for the phases [59]. As seen from Fig. 6 d, the phases of Ti_2AB has the highest heat transport while Hf_2AB exhibits relatively low thermal conductivity. In order to support the deduced results, we have calculated the thermal conductivities of M_2AB by using two theoretical methods: Clarke's model [60,61] and Cahill's model [62]. The formula used as in Ref. [63]. The obtained results are given in Table 6. And, it indicates that they are convince with the results obtained from acoustic branches.

It is seen in Fig. 6, which show the DOS, the phonon dispersion curves can be separated into two main regions. This difference between the optical branches is due to the difference in the mass between atoms.

The main contributions to the optic branches in the region belong to lower frequencies than about 10 THz come from the M and A atoms. And the dominant contribution comes from M atoms. In the region of higher frequencies, optic branches mainly arise from the borides atoms.

Additionally, the phonon frequencies at Γ point for all compounds have been listed in Table 7. The classification of the phonon modes for this material can be given as; A_{1g}+$3A_{2u}$+$2B_{1g}$+$2B_{2u}$+$2E_{2u}$+$2E_{2g}$+$3E_{1u}$+E_{1g}.

Here, A_{2u}+E_{1u} belongs to acoustic phonon modes and the others belong to varied optic phonon modes. These optic modes are Raman Active Modes (Γ_R = A_{1g}+E_{1g}+$2E_{2g}$), Hyper Raman Active Modes (Γ_H = $2B_{1g}$+$2B_{2u}$+$2E_{2u}$) and Infrared Active Modes (Γ_I = $2A_{2u}$ + $2E_{1u}$).

Phonon frequencies of these compounds at Γ point can provide useful information for future experiments to identify the predicted new phases.

4. Conclusions

The structural, electronic, mechanical, and lattice dynamical properties for hypothetical M_2AB phases have been investigated. The calculated negative formation enthalpy shows that all M_2AB phases are thermodynamically stable under ambient conditions and Hf_2InB possesses the lowest formation enthalpy. The band structures for all phases are also metallic in nature. The obtained DOS and charge density maps show that all phases dominantly have ionic in nature.

The calculated elastic constants have also indicated that M_2AB are mechanically stable. Moreover, the compounds of M = *Zr* have brittleness behavior and the compounds of M = *Ti* and *Hf* have ductility behavior. In addition, except from the *Zr* involved compounds and Hf_2GaB compound, M_2AB phases are relatively hard materials, and Ti_2AlB is the hardnest phase.

The obtained structural, electronic, and elastic properties of M_2AlB (M = *Ti, Zr,* and *Hf*) are also in a good agreement with available theoretical results.

Phonon curves and corresponding PDOS graphics of M_2AB phases reveal that any negative mode has not been found to indicate the dynamical stability of the materials. The thermal conductivities of M_2AB which are evaluated via Clarke's and Cahill's model indicate that these phases possess a relatively lower thermal conductivity.

As a result, M_2AB phases can be considered as a candidate for the family of M_2AX phases and it is hoped that, these systematic calculations and analysis of the structural, electronic, mechanical, and lattice dynamical properties for hypothetical M_2AB phases reported here could be useful in the future design of new materials with borides.

References

[1] M.W. Barsoum, M. Radovic, Elastic and mechanical properties of the MAX phases, Annu. Rev. Mater. Res. 41 (2011) 195–227, https://doi.org/10.1146/annurev-matsci-062910-100448.
[2] Z.M. Sun, Progress in research and development on MAX phases: a family of

layered ternary compounds, Int. Mater. Rev. 56 (2011) 143–166, https://doi.org/10.1179/1743280410Y.0000000001.
[3] B. Ghebouli, M.A. Ghebouli, M. Fatmi, L. Louail, T. Chihi, A. Bouhemadou, First-principles calculations of structural, electronic, elastic and thermal properties of phase M2SiC (M=Ti, V, Cr, Zr, Nb, Mo, Hf, Ta and W), Trans. Nonferrous Met. Soc. China 25 (2015) 915–925, https://doi.org/10.1016/S1003-6326(15)63680-9.
[4] M.A. Ali, M.S. Ali, M.M. Uddin, Structural, elastic, electronic and optical properties of metastable MAX phase Ti5SiC4 compound, Indian J. Pure Appl. Phys. 54 (2016) 386–390. http://op.niscair.res.in/index.php/IJPAP/article/view/4502.
[5] M.F. Cover, O. Warschkow, M.M.M. Bilek, D.R. McKenzie, Elastic properties of Ti n +1 AlC n and Ti n +1 AlN n MAX phases, Adv. Eng. Mater 10 (2008) 935–938, https://doi.org/10.1002/adem.200800109.
[6] J. Xu, M.-Q. Zhao, Y. Wang, W. Yao, C. Chen, B. Anasori, A. Sarycheva, C.E. Ren, T. Mathis, L. Gomes, L. Zhenghua, Y. Gogotsi, Demonstration of Li-Ion capacity of MAX phases, ACS Energy Lett. 1 (2016) 1094–1099, https://doi.org/10.1021/acsenergylett.6b00488.
[7] A.S. Ingason, M. Dahlqvist, J. Rosen, Magnetic MAX phases from theory and experiments; a review, J. Phys. Condens. Matter 28 (2016) 433003, https://doi.org/10.1088/0953-8984/28/43/433003.
[8] H. Högberg, L. Hultman, J. Emmerlich, T. Joelsson, P. Eklund, J.M. Molina-Aldareguia, J.-P. Palmquist, O. Wilhelmsson, U. Jansson, Growth and characterization of MAX-phase thin films, Surf. Coatings Technol. 193 (2005) 6–10, https://doi.org/10.1016/j.surfcoat.2004.08.174.
[9] D. Horlait, S.C. Middleburgh, A. Chroneos, W.E. Lee, Synthesis and DFT investigation of new bismuth-containing MAX phases, Sci. Rep. 6 (2016) 18829, https://doi.org/10.1038/srep18829.
[10] M. Dahlqvist, B. Alling, J. Rosén, Stability trends of MAX phases from first principles, Phys. Rev. B - Condens. Matter Mater. Phys. 81 (2010) 1–4, https://doi.org/10.1103/PhysRevB.81.220102.
[11] G. Surucu, K. Colakoglu, E. Deligoz, N. Korozlu, First-Principles Study on the MAX Phases Ti n+1GaN n (n = 1,2, and 3), J. Electron. Mater 45 (2016) 4256–4264, https://doi.org/10.1007/s11664-016-4607-1.
[12] M. Roknuzzaman, M.A. Hadi, M.J. Abden, M.T. Nasir, A.K.M.A. Islam, M.S. Ali, K. Ostrikov, S.H. Naqib, Physical properties of predicted Ti2CdN versus existing Ti2CDC MAX phase: an ab initio study, Comput. Mater. Sci. 113 (2016) 148–153, https://doi.org/10.1016/j.commatsci.2015.11.039.
[13] C. Lange, M.W. Barsoum, P. Schaaf, Towards the synthesis of MAX-phase functional coatings by pulsed laser deposition, Appl. Surf. Sci. 254 (2007) 1232–1235, https://doi.org/10.1016/j.apsusc.2007.07.156.
[14] I.R. Shein, A.L. Ivanovskii, Elastic properties of superconducting MAX phases from first-principles calculations, Phys. Status Solidi 248 (2011) 228–232, https://doi.org/10.1002/pssb.201046163.
[15] J. Wang, Z. Liu, H. Zhang, J. Wang, Tailoring magnetic properties of MAX phases, a theoretical investigation of (Cr2Ti)AlC2 and Cr2AlC, J. Am. Ceram. Soc. 3375 (2016) 3371–3375, https://doi.org/10.1111/jace.14358.
[16] D.W. Clark, S.J. Zinkle, M.K. Patel, C.M. Parish, High temperature ion irradiation effects in MAX phase ceramics, Acta Mater 105 (2016) 130–146, https://doi.org/10.1016/j.actamat.2015.11.055.
[17] D.J. Tallman, E.N. Hoffman, E.N. Caspi, B.L. Garcia-Diaz, G. Kohse, R.L. Sindelar, M.W. Barsoum, Effect of neutron irradiation on select MAX phases, Acta Mater 85 (2015) 132–143, https://doi.org/10.1016/j.actamat.2014.10.068.
[18] P. Eklund, M. Dahlqvist, O. Tengstrand, L. Hultman, J. Lu, N. Nedfors, U. Jansson, J. Rosén, Discovery of the ternary nanolaminated compound Nb2GeC by a systematic theoretical-experimental, Phys. Rev. Lett. 109 (2012) 35502, https://doi.org/10.1103/PhysRevLett.109.035502.
[19] C. Hu, H. Zhang, F. Li, Q. Huang, Y. Bao, New phases' discovery in MAX family, Int. J. Refract. Met. Hard Mater 36 (2013) 300–312, https://doi.org/10.1016/j.ijrmhm.2012.10.011.
[20] M. Naguib, G.W. Bentzel, J. Shah, J. Halim, E.N. Caspi, J. Lu, L. Hultman, M.W. Barsoum, New solid solution MAX phases: (Ti0.5, V0.5)3AlC2, (Nb0.5, V0.5)2AlC, (Nb0.5, V0.5)4AlC3 and (Nb0.8, Zr0.2)2AlC, Mater. Res. Lett. 2 (2014) 233–240, https://doi.org/10.1080/21663831.2014.932858.
[21] A.S. Ingason, A. Petruhins, M. Dahlqvist, F. Magnus, A. Mockute, B. Alling, L. Hultman, I.A. Abrikosov, P.O.Å. Persson, J. Rosen, A nanolaminated magnetic phase: Mn 2 GaC, Mater. Res. Lett. 2 (2014) 89–93, https://doi.org/10.1080/21663831.2013.865105.
[22] T. Lapauw, K. Lambrinou, T. Cabioc'h, J. Halim, J. Lu, A. Pesach, O. Rivin, O. Ozeri, E.N. Caspi, L. Hultman, P. Eklund, J. Rosén, M.W. Barsoum, J. Vleugels, Synthesis of the new MAX phase Zr2AlC, J. Eur. Ceram. Soc. 36 (2016) 1847–1853, https://doi.org/10.1016/j.jeurceramsoc.2016.02.044.
[23] L. Zheng, J. Wang, X. Lu, F. Li, J. Wang, Y. Zhouw, (Ti0.5Nb0.5)5AlC4: a new-layered compound belonging toMAX phases, J. Am. Ceram. Soc. 93 (2010) 3068–3071, https://doi.org/10.1111/j.1551-2916.2010.04056.x.
[24] B. Anasori, J. Halim, J. Lu, C.A. Voigt, L. Hultman, M.W. Barsoum, Mo2TiAlC2: a new ordered layered ternary carbide, Scr. Mater. 101 (2015) 5–7, https://doi.org/10.1016/j.scriptamat.2014.12.024.
[25] C. Xu, H. Zhang, S. Hu, X. Zhou, S. Peng, H. Xiao, G. Zhang, First-principles calculations of Ti3SiC2 and Ti3AlC2 with hydrogen interstitial, J. Nucl. Mater (2016), https://doi.org/10.1016/j.jnucmat.2016.09.025.
[26] M. Dahlqvist, Benefits of oxygen incorporation in atomic laminates, J. Phys. Condens. Matter 28 (2016) 135501, https://doi.org/10.1088/0953-8984/28/13/135501.
[27] H. Ding, N. Glandut, X. Fan, Q. Liu, Y. Shi, J. Jie, First-principles study of hydrogen incorporation into the MAX phase Ti3AlC2, Int. J. Hydrogen Energy 41 (2016) 6387–6393, https://doi.org/10.1016/j.ijhydene.2016.03.015.
[28] Y. Zhang, S. Yang, C. Wang, First-principles calculations for point defects in MAX phases Ti 2 AlN, Mod. Phys. Lett. B 30 (2016) 1650101, https://doi.org/10.1142/S0217984916501013.
[29] A.G. Zhou, M.W. Barsoum, Kinking nonlinear elastic deformation of Ti3AlC2, Ti2AlC, Ti3Al(C0.5,N0.5)2 and Ti2Al(C0.5,N0.5), J. Alloys Compd. 498 (2010) 62–70, https://doi.org/10.1016/j.jallcom.2010.03.099.
[30] M. Radovic, A. Ganguly, M.W. Barsoum, Elastic properties and phonon conductivities of Ti3Al(C0.5,N0.5)2 and Ti2Al(C0.5,N0.5) solid solutions, J. Mater. Res. 23 (2008) 1517–1521, https://doi.org/10.1557/JMR.2008.0200.
[31] B. Manoun, S.K. Saxena, G. Hug, A. Ganguly, E.N. Hoffman, M.W. Barsoum, Synthesis and compressibility of Ti3(Al,Sn0.2)C2 and Ti3Al(C0.5,N0.5)2, J. Appl. Phys. 101 (2007) 113523/1–113523/7, https://doi.org/10.1063/1.2733644.
[32] M. Khazaei, M. Arai, T. Sasaki, M. Estili, Y. Sakka, Trends in electronic structures and structural properties of MAX phases: a first-principles study on M(2)AlC (M = Sc, Ti, Cr, Zr, Nb, Mo, Hf, or Ta), M(2)AlN, and hypothetical M(2)AlB phases, J. Phys. Condens. Matter 26 (2014) 505503, https://doi.org/10.1088/0953-8984/26/50/505503.
[33] O.O. Kurakevych, Superhard phases of simple substances and binary compounds of the B-C-N-O system: from diamond to the latest results (a Review), J. Superhard Mater 31 (2009) 139–157, https://doi.org/10.3103/S1063457609030010.
[34] G. Kresse, J. Furthmüller, Efficiency of ab-initio total energy calculations for metals and semiconductors using a plane-wave basis set, Comput. Mater. Sci. 6 (1996) 15–50, https://doi.org/10.1016/0927-0256(96)00008-0.
[35] G. Kresse, J. Furthmüller, Efficient iterative schemes for ab initio total-energy calculations using a plane-wave basis set, Phys. Rev. B 54 (1996) 11169–11186, https://doi.org/10.1103/PhysRevB.54.11169.
[36] G. Kresse, From ultrasoft pseudopotentials to the projector augmented-wave method, Phys. Rev. B 59 (1999) 1758–1775, https://doi.org/10.1103/PhysRevB.59.1758.
[37] P.E. Blöchl, Projector augmented-wave method, Phys. Rev. B 50 (1994) 17953–17979, https://doi.org/10.1103/PhysRevB.50.17953.
[38] J.P. Perdew, K. Burke, M. Ernzerhof, Generalized gradient approximation made simple, Phys. Rev. Lett. 77 (1996) 3865–3868, https://doi.org/10.1103/PhysRevLett.77.3865.
[39] J.D. Pack, H.J. Monkhorst, "special points for Brillouin-zone integrations"-a reply, Phys. Rev. B 16 (1977) 1748–1749, https://doi.org/10.1103/PhysRevB.16.1748.
[40] M. Methfessel, A.T. Paxton, High-precision sampling for Brillouin-zone integration in metals, Phys. Rev. B 40 (1989) 3616–3621, https://doi.org/10.1103/PhysRevB.40.3616.
[41] P.E. Blöchl, O. Jepsen, O.K. Andersen, Improved tetrahedron method for Brillouin-zone integrations, Phys. Rev. B 49 (1994) 16223–16233, https://doi.org/10.1103/PhysRevB.49.16223.
[42] Le Page, Y.; Saxe, P.. Symmetry-general least-squares extraction of elastic data for strained materials from ab initio calculations of stress, (n.d.). doi:10.1103/PhysRevB.65.104104.
[43] X. Gonze, C. Lee, Dynamical matrices, Born effective charges, dielectric permittivity tensors, and interatomic force constants from density-functional perturbation theory, Phys. Rev. B 55 (1997) 10355–10368, https://doi.org/10.1103/PhysRevB.55.10355.
[44] A. Togo, F. Oba, I. Tanaka, First-principles calculations of the ferroelastic transition between rutile-type and CaCl 2 -type SiO 2 at high pressures, Phys. Rev. B 78 (2008) 134106, https://doi.org/10.1103/PhysRevB.78.134106.
[45] K. Momma, F. Izumi, P.M. J., P.C. J., H.P. J., C.S. J., P.M. C., N. T., K. Y., *VESTA 3* for three-dimensional visualization of crystal, volumetric and morphology data, J. Appl. Crystallogr. 44 (2011) 1272–1276, https://doi.org/10.1107/S0021889811038970.
[46] J.H. Xu, A.J. Freeman, Band filling and structural stability of cubic tri-aluminides: YAl3, ZrAl3, and NbAl3, Phys. Rev. B 40 (1989) 11927–11930, https://doi.org/10.1103/PhysRevB.40.11927.
[47] J.-H. Xu, T. Oguchi, A.J. Freeman, Crystal structure, phase stability, and magnetism in Ni3V, Phys. Rev. B 35 (1987) 6940–6943, https://doi.org/10.1103/PhysRevB.35.6940.
[48] Z. Wu, E. Zhao, H. Xiang, X. Hao, X. Liu, J. Meng, Crystal structures and elastic properties of superhard IrN2 and IrN3 from first principles, Phys. Rev. B 76 (2007) 54115, https://doi.org/10.1103/PhysRevB.76.054115.
[49] R.-K. Pan, L. Ma, N. Bian, M.-H. Wang, P.-B. Li, B.-Y. Tang, L.-M. Peng, W.-J. Ding, First-principles study on the elastic properties of B′ and Q phase in Al–Mg–Si (–Cu) alloys, Phys. Scr 87 (2013) 15601, https://doi.org/10.1088/0031-8949/87/01/015601.
[50] A. Reuss, Berechnung der Fließgrenze von Mischkristallen auf Grund der Plastizitätsbedingung für Einkristalle, ZAMM - J. Appl. Math. Mech./Zeitschrift Für Angew. Math. Und Mech. 9 (1929) 49–58, https://doi.org/10.1002/zamm.19290090104.
[51] R. Hill, The elastic behaviour of a crystalline aggregate, Proc. Phys. Soc. Sect. A 65 (1952) 349–354, https://doi.org/10.1088/0370-1298/65/5/307.
[52] V.V. Bannikov, I.R. Shein, A.L. Ivanovskii, Electronic structure, chemical bonding and elastic properties of the first thorium-containing nitride perovskite TaThN3, Phys. Status Solidi – Rapid Res. Lett. 1 (2007) 89–91, https://doi.org/10.1002/pssr.200600116.
[53] X.-Q. Chen, H. Niu, D. Li, Y. Li, Modeling hardness of polycrystalline materials

and bulk metallic glasses, Intermetallics 19 (2011) 1275–1281, https://doi.org/10.1016/j.intermet.2011.03.026.
[54] H. Ledbetter, A. Migliori, A general elastic-anisotropy measure, J. Appl. Phys. 100 (2006), https://doi.org/10.1063/1.2338835.
[55] J. Chang, G.-P. Zhao, X.-L. Zhou, K. Liu, L.-Y. Lu, Structure and mechanical properties of tantalum mononitride under high pressure: a first-principles study, J. Appl. Phys. 112 (2012) 83519, https://doi.org/10.1063/1.4759279.
[56] A. Marmier, Z.A.D. Lethbridge, R.I. Walton, C.W. Smith, S.C. Parker, K.E. Evans, ElAM: a computer program for the analysis and representation of anisotropic elastic properties, Comput. Phys. Commun. 181 (2010) 2102–2115, https://doi.org/10.1016/j.cpc.2010.08.033.
[57] H. Fu, W. Liu, Y. Ma, T. Gao, Prediction study of the axial compressibility, anisotropy and dynamic properties for single crystal Ti 2 GeC, J. Alloys Compd. 506 (2010) 22–26, https://doi.org/10.1016/j.jallcom.2010.06.186.
[58] N. Miao, B. Sa, J. Zhou, Z. Sun, Theoretical investigation on the transition-metal borides with Ta 3 B 4 -type structure: a class of hard and refractory materials, Comput. Mater. Sci. 50 (2011) 1559–1566, https://doi.org/10.1016/j.commatsci.2010.12.015.
[59] H. Shao, X. Tan, T. Hu, G.-Q. Liu, J. Jiang, H. Jiang, First-principles study on the lattice dynamics and thermodynamic properties of Cu_2GeSe_3, EPL Europhys. Lett. 109 (2015) 47004, https://doi.org/10.1209/0295-5075/109/47004.
[60] D.R. Clarke, Materials selection guidelines for low thermal conductivity thermal barrier coatings, Surf. Coatings Technol. 163–164 (2003) 67–74, https://doi.org/10.1016/S0257-8972(02)00593-5.
[61] D.R. Clarke, C.G. Levi, Materials desing for the next generation thermal barrier coanings, Annu. Rev. Mater. Res. 33 (2003) 383–417, https://doi.org/10.1146/annurev.matsci.33.011403.113718.
[62] D.G. Cahill, S.K. Watson, R.O. Pohl, Lower limit to the thermal conductivity of disordered crystals, Phys. Rev. B 46 (1992) 6131–6140, https://doi.org/10.1103/PhysRevB.46.6131.
[63] E. Deligoz, H. Ozisik, Mechanical and dynamical stability of TiAsTe compound from ab initio calculations, Philos. Mag. 95 (2015) 2294–2305, https://doi.org/10.1080/14786435.2015.1056854.